Copper oxide as a synergistic catalyst for the oxygen reduction reaction on La$_{0.6}$Sr$_{0.4}$Co$_{0.2}$Fe$_{0.8}$O$_{3-\delta}$ perovskite structured electrocatalyst

CrossMark

Tao Hong [a, b], Kyle Brinkman [b], Changrong Xia [a, *]

[a] Key Laboratory of Materials for Energy Conversion, Chinese Academy of Sciences, Department of Materials Science and Engineering & Collaborative Innovation Center of Suzhou Nano Science and Technology, University of Science and Technology of China, No. 96 Jinzhai Road, Hefei, Anhui Province, 230026, PR China
[b] Department of Materials Science and Engineering, Clemson University, Clemson, SC29634, USA

H I G H L I G H T S

- CuO is used as synergistic catalyst for oxygen reduction reaction on LSCF.
- Enhanced rate is attributed to CuO surface and LSCF-CuO-gas boundaries.
- The contribution of CuO to incorporated oxygen could reach 78%.
- The reduced resistance of LSCF is related to oxygen surface process.
- LSCF and CuO could remain chemical compatible in testing condition.

A R T I C L E   I N F O

A B S T R A C T

This work presents the effect of dispersed copper oxide (CuO) nanoparticles on the oxygen reduction reaction (ORR) on a typical solid oxide fuel cell (SOFC) electrocatalyst, La$_{0.6}$Sr$_{0.4}$Co$_{0.2}$Fe$_{0.8}$O$_{3-\delta}$ (LSCF). The ORR kinetics were enhanced by a factor up to 4 at 750 °C as demonstrated by electrical conductivity relaxation measurements used to determine the chemical surface exchange coefficient, k_{chem}. The value of k_{chem} increased from 2.6×10^{-5} cm s^{-1} to 9.3×10^{-5} cm s^{-1} at 750 °C when the LSCF surface was coated with submicron CuO particles. The enhanced k_{chem} was attributed to additional reactions that occur on the CuO surface and at the LSCF-CuO-gas three-phase boundaries (3PBs) as suggested by the k_{chem} dependence on CuO coverage and 3PB length. This enhancement was further demonstrated by the introduction of CuO nanoparticles into LSCF electrodes. CuO infiltrated electrodes reduced the interfacial polarization resistance from 2.27 Ω cm^2 to 1.5 Ω cm^2 at 600 °C and increased the peak power density from 0.54 W cm^{-2} to 0.72 W cm^{-2} at 650 °C. Electrochemical impedance spectroscopy indicated that the reduced resistance was due to the shrinkage of the low frequency arc, which is associated with the electrochemical surface exchange reaction.

© 2016 Elsevier B.V. All rights reserved.

1. Introduction

La$_{0.6}$Sr$_{0.4}$Co$_{0.2}$Fe$_{0.8}$O$_{3-\delta}$ (LSCF) is a mixed ionic and electronic conductive (MIEC) perovskite oxide which has demonstrated excellent catalytic activity for the oxygen reduction reaction (ORR) in addition to high level of ion/electron conductivities which have attracted considerable attention for applications including solid oxide fuel cell (SOFCs) cathodes, oxygen sensors, and oxygen separation membranes [1–3]. While significant progress has been made on LSCF based electrocatalysts, there is still room for improvement in order to achieve enhanced chemical-to-electrical conversion efficiency [4,5]. Efforts have been made to develop nano-scale and nano-structured electrodes, which are usually achieved by an impregnation or infiltration method. The unique structure of nanoparticles on the surface of submicron LSCF grains results in an enlarged surface area for three-phase boundaries (3PBs) where the electrode catalyst, electrolyte and gas phases

meet and catalytic reaction occur [6,7]. Traditionally, costly precious metals such as Ag [8,9], Pd [10] and Rh [11] were used as nanoparticles to enhance the activity, i.e. reduce the interfacial polarization resistance of LSCF based cathodes used in SOFCs. Due to concurrent issues of the high cost of Pt and performance degradation associated with metal particle coarsening, alternative catalysts based on non-precious metals and metal-free materials are being actively pursued. Recent examples are the infiltration of oxides such as doped ceria $Sm_{0.2}Ce_{0.8}O_{2-\delta}$ (SDC) [12] and $Gd_{0.1}Ce_{0.9}O_{2-\delta}$ (GDC) [13] which have been reported to improve the ORR catalytic activity. The performance improvements observed in doped ceria which has high levels of oxygen ion conductivity have been attributed to the enlarged 3PB where ORR principally occurs [14]. Hu et al. [15,16] have used an electrical conductivity relaxation (ECR) method to determine the ORR kinetics at the LSCF-SDC boundary. It was found that the oxygen incorporation at the LSCF-SDC-gas 3PB was more facile than on the LSCF surface. Estimates for the individual contributions of 3PB and LSCF surface indicated that the 3PB zones contribute 70% of the total ORR on the dense LSCF-SDC composite. In addition active metals and oxygen-ion conductive oxides, materials such as Co_3O_4 and $BaCO_3$ have been tried as nanoparticle coatings to improve ORR activity through synergistic effects [17,18]. For example, $BaCO_3$ nanoparticles were recently demonstrated as excellent synergistic catalytic materials resulting in significant improvements in the ORR reaction in intermediate-temperature SOFCs. The performance improving factors of $BaCO_3$ nanoparticles were found to be even higher than those reported for precious metals [19]. Subsequent work revealed that the enhanced electrochemical performance is mainly associated with the surface exchange process [20].

Transition metal oxides such as CuO are often considered as optimal catalysts for CO oxidation [21—23]. This material has not attracted much attention for the reduction reaction because of the perceived limited catalytic abilities towards ORR. Chang et al. have reported the application of CuO as the cathode materials for $Y_{0.15}Zr_{0.85}O_{2-\delta}$ (YSZ) electrolyte [24] and proposed that CuO may posses requisite levels of oxygen vacancies needed to serve as a MIEC. CuO has also been used as a sintering aid to reduce the electrode calcination temperature [25]. In this work, it was found that 2 mol% CuO added to a LSCF-SDC composite, reduced the calcination temperature from 1000 °C to 800 °C and resulted in a 67% higher performance with an area specific resistance is 0.05 Ω cm² at 700 °C.

This work reports on an investigation of the synergistic catalytic effect of CuO for ORR on LSCF electrodes. An ECR method was employed to investigate CuO effect on the ORR kinetics, i.e. the chemical surface oxygen exchange coefficient k_{Chem}. Combined with the surface microstructure analysis, we reveal the relationship between k_{Chem} and CuO surface morphology data and quantify the contribution of CuO to the overall oxygen incorporation rate. The performance of dispersed copper oxide (CuO) nanoparticles on LSCF electrodes was evaluated to verify the enhanced surface reaction process.

2. Experiment

2.1. Powder preparation

LSCF ($La_{0.6}Sr_{0.4}Co_{0.2}Fe_{0.8}O_{3-\delta}$) powder was prepared with citric-EDTA method [26]. Stoichiometric amounts of precursors $La(NO_3)_3*6H_2O$, $Sr(NO_3)_2$, $Co(NO_3)_3*6H_2O$ and $Fe(NO_3)_3*9H_2O$ (Sinopharm Chemical Reagent Co. Ltd) were dissolved in distilled water. Citric acid was then added to the solution at a mole ratio of 1:1:1 for metal ions: citric: EDTA and the pH value of the solution was controlled in 7 by using ammonia water at last. The precursor solution was subsequently heated on a hot plate until self-combustion occurred. The resulting ashes were calcined at 800 °C for 2 h to remove possible organic residues and to form the desired perovskite structure. SDC ($Sm_{0.2}Ce_{0.8}O_{1.9}$) and NiO powders were prepared with the glycine-nitrate process and followed by heating the ashes at 600 and 850 °C for 2 h, respectively. To test the chemical compatibility of LSCF with the CuO, LSCF powders were mixed with $Cu(NO_3)_2*3H_2O$ at the weight ratio of 1:1 and sintered at 800 °C for 10 h.

2.2. Cell fabrications

Symmetrical cells were composed of dense SDC electrolyte substrates and porous LSCF electrodes decorated with CuO particles. The SDC powders were die-pressed at 250 MPa to form green substrates with a diameter of 13 mm and subsequently sintered at 1300 °C for 5 h. LSCF slurries were prepared by mixing the LSCF powders with an organic binder (α-terpineol as solvent and ethyl cellulose as the binder). The slurries were then printed onto both sides of the substrates. After drying under an infrared lamp, the samples were heated at 1000 °C for 2 h to form symmetrical cell structures. In order to infiltrate CuO particles, a solution was prepared with $Cu(NO_3)_2*3H_2O$ dissolved in a mixture of water and ethanol (2:1, v/v) at a metal ions concentration of 0.3 mol L^{-1}. The infiltrating process was carried out by placing a drop of the solution on the top of the porous LSCF, letting the solution soak into the porous structure, drying, and heating the sample at 800 °C in air for 1 h to form metal oxide particles. The sample mass before and after each impregnating-drying-heating cycle was measured to estimate the CuO loading, which was expressed as the mass ratio of the infiltrated oxides to the porous LSCF.

Single cells were fabricated with the configuration of NiO-SDC anode substrates, SDC film electrolytes, and LSCF cathodes. The anode powders consisting of 65 wt% NiO and SDC were combined, and 20 wt% graphite was added as the pore forming—agent followed by pressing at 30 MPa. SDC powder as the electrolyte was subsequently added on the top of the pre-pressed anode pellet and co-pressed at 180 MPa to form a green bi-layer structure. The green bodies were sintered at 1300 °C for 5 h to densify the electrolyte layer. Cathodes were fabricated on the electrolytes with the same process used for symmetrical cell fabrication previously described.

Table 1
Characteristics for CuO particles on LSCF surfaces.

Sample code	Sputter time (s)	Processing temperature (°C)	θ_{CuO}	L_{3PB} (μm^{-1})	k_{eff} at 750 °C ($\times 10^{-5}$ cm s^{-1})
Bare LSCF	0	—	0	0	2.6
CuO40	40	800	0.00792	1.13576	4.0
CuO60	60	800	0.02809	2.6102	5.8
CuO80	80	800	0.054	5.22519	7.23
CuO100	100	800	0.1279	12.6139	9.05
CuO120	120	800	0.1354	14.74012	9.3
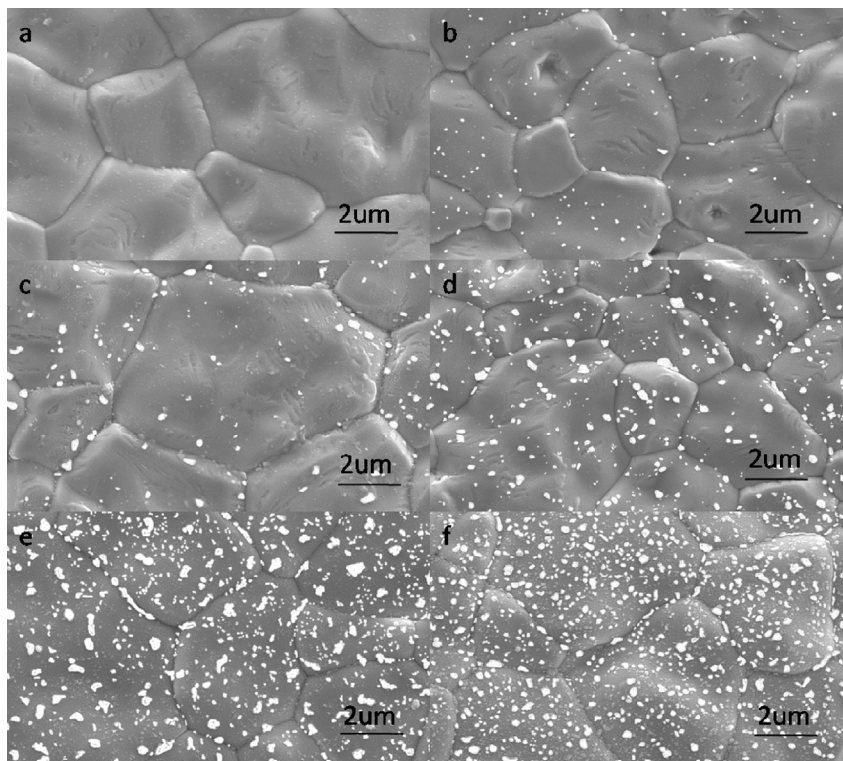
Fig. 1. Surface SEM micrographs for (a) a bare LSCF bar and LSCF bars deposited with CuO for (b) 40 s, (c) 60 s, (d) 80 s, (e) 100 s and (f) 120 s. The micrograph was treated with ImageJ to obtain θ_{CuO} and L_{3PB}.

2.3. Sample characterization

The phase structure was characterized by X-ray diffraction (Rigaku TTR-III) analysis using Cu K radiation (D/Max-gA, 2 kV) with 2θ from 20 to 80° with a scan rate of 3° per minute. The morphology of the cell was observed using a scanning electron microscope (SEM, JEOL JSM-6700F) and transition electron microscope (TEM, JEOL JSM-2010). The phase of CuO nano-particle was confirmed by energy dispersive spectrometer (EDS). The surface area and length of the CuO in LSCF surface were obtained using the image analysis software ImageJ [15]. For each sample, images from at least three different areas of the sample were used to obtain average values of particle size, length of the CuO-LSCF-gas 3PB and surface area of LSCF and CuO. Electrochemical measurements were carried out with a Zahner Im6e electrochemical workstation under open circuit conditions. Ag paste and Ag wires were used to make electrical contact with the electrode materials. The impedance of a symmetric cell was measured in ambient air, and the frequency ranged from 10^{-1} to 10^6 Hz with an AC signal amplitude of 10 mV. AC impedance plots were fitted using Zview software according to proper equivalent circuit with a standard deviation below 5%. The performance of the single cell was evaluated using humidified (~3% H_2O) hydrogen as the fuel with a flow rate of 25 ml min^{-1} and ambient air as the oxidant. All impedance spectra for single cells were recorded under open-circuit conditions with 10 mV AC signal perturbation.

2.4. Electrical conductivity relaxation experiment

To conduct the ECR measurement, the LSCF powders were ground, pressed into a rectangular bar at 300 MPa, and sintered at 1400 °C for 5 h in air to form dense LSCF samples [19]. The size of the sintered bars had dimensions of 40.00 × 5.42 × 0.90 mm³. All sintered samples were confirmed to possess a density in excess of 95% of the theoretical density determined using the Archimedes method. Cu metal particles were deposited on the bar surfaces using sputter deposition (JFC-1600, JEOL) at 20 mA under the vacuum of 8 Pa, followed by heating at 800 °C to form CuO particles. Details of the synthesis process are summarized in Table 1. The conductivity was measured by a standard, four-probe method using a measurement system consisting of a digital multimeter (Keithley 2001) interfaced for data collection by the use of custom LABVIEW 8.5 software. During the ECR measurements, the gas phase atmosphere changed from $Po_2 = 0.01$ bar ($O_2 + N_2$) to $Po_2 = 0.1$ bar ($O_2 + N_2$) with additional experimental details described in prior publications [16]. The change in conductivity with time is plotted as $(\sigma(t) - \sigma(0))/(\sigma(\infty) - \sigma(0))$, where $\sigma(0)$, $\sigma(t)$ and $\sigma(\infty)$ denote the initial, time dependent and final conductivities, respectively. The experimental data is fitted to the theoretical equations as outlined by Lane and Kilner [27] for conductivity relaxation to derive the oxygen surface exchange and the oxygen diffusion coefficients.

3. Results and discussion

3.1. Surface structure of CuO decorated LSCF bar

Fig. 1 shows the surface microstructures of the CuO decorated LSCF bar. The relative density of the bare LSCF bar (Fig. 1a) is 97% as determined with the Archimedes method in distilled water, which is high enough for the ECR measurement [27]. Fig. 1b–f are the typical micro views for LSCF surfaces with CuO particles. The particles appear disconnected, and are distributed uniformly on LSCF surface. The SEM pictures were statistically analyzed to obtain the CuO–LSCF boundary length per unit area, i.e. the 3PB line density L_{3PB}, which increased with an increase of Cu sputtering time up to 120 s. The surface coverage of CuO particles (θ_{CuO}) was also found to

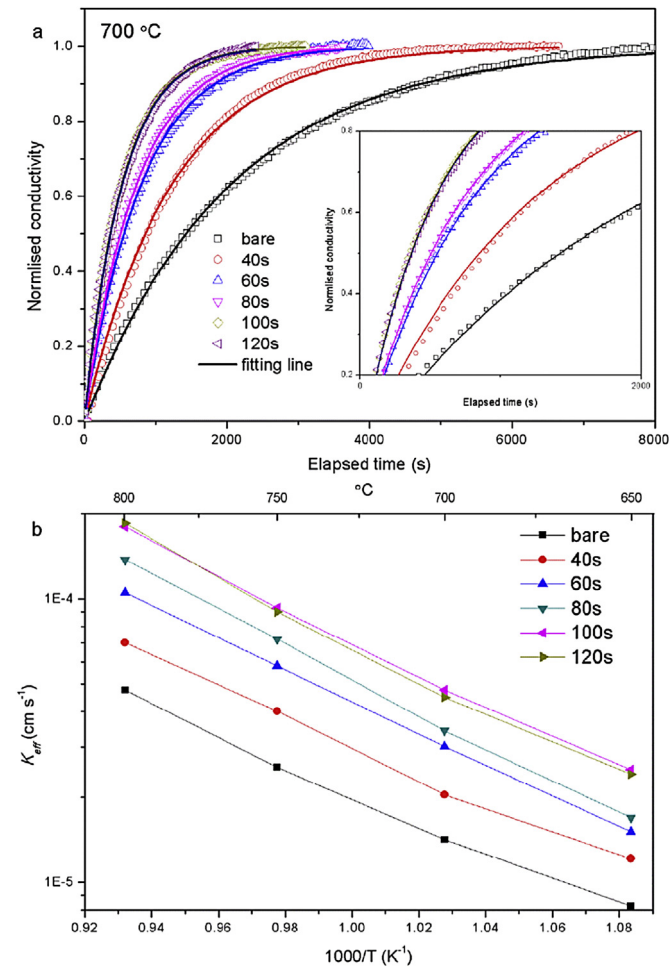**Fig. 2.** (a) Normalized conductivity data and fitting curves and (b) chemical oxygen surface exchange coefficients (k_{eff}) for LSCF decorated with CuO.

increase with the sputtering time. Data for these experimental are listed in Table 1.

3.2. Effect of CuO decoration on ORR kinetics

Fig. 2a displays the normalized conductivity at 700 °C versus the elapsed time. It is clear that the equilibrium time, representing reaction completion after the oxygen partial pressure was changed from 0.01 to 0.1 bar, is about 8000 s for the bare LSCF bar. It is effectively reduced by the addition of CuO particles on the surface. At CuO levels controlled by the time of sputtering deposition for 40 s, the equilibrium time was reduced to 6000 s. It was further reduced to 2500 s using increased CuO surface coverage with sputtering deposition time of 120 s Fig. 2a also shows the curves for the elapsed time less than 2000 s which clearly indicate the CuO effect. The incorporation of oxygen from a gas phase into the bulk of a solid phase has been researched for many years. In summary, the kinetics of the oxygen exchange reaction may be coupled to molecular diffusion and surface transport processes, as well as to bulk ionic and electronic transport. At the first, O^2 from gas are adsorbed to LSCF surface, then dissociated to oxygen atoms. The oxygen atoms get electrons and oxygen vacancies from LSCF lattice and incorporated as lattice oxygen. In LSCF bulk, the lattice oxygen transports from LSCF edge to middle site. Finally, oxygen concentration in LSCF bulk reaches homogeneous. At the same time, oxygen in LSCF bulk stays balance with atmosphere. In our
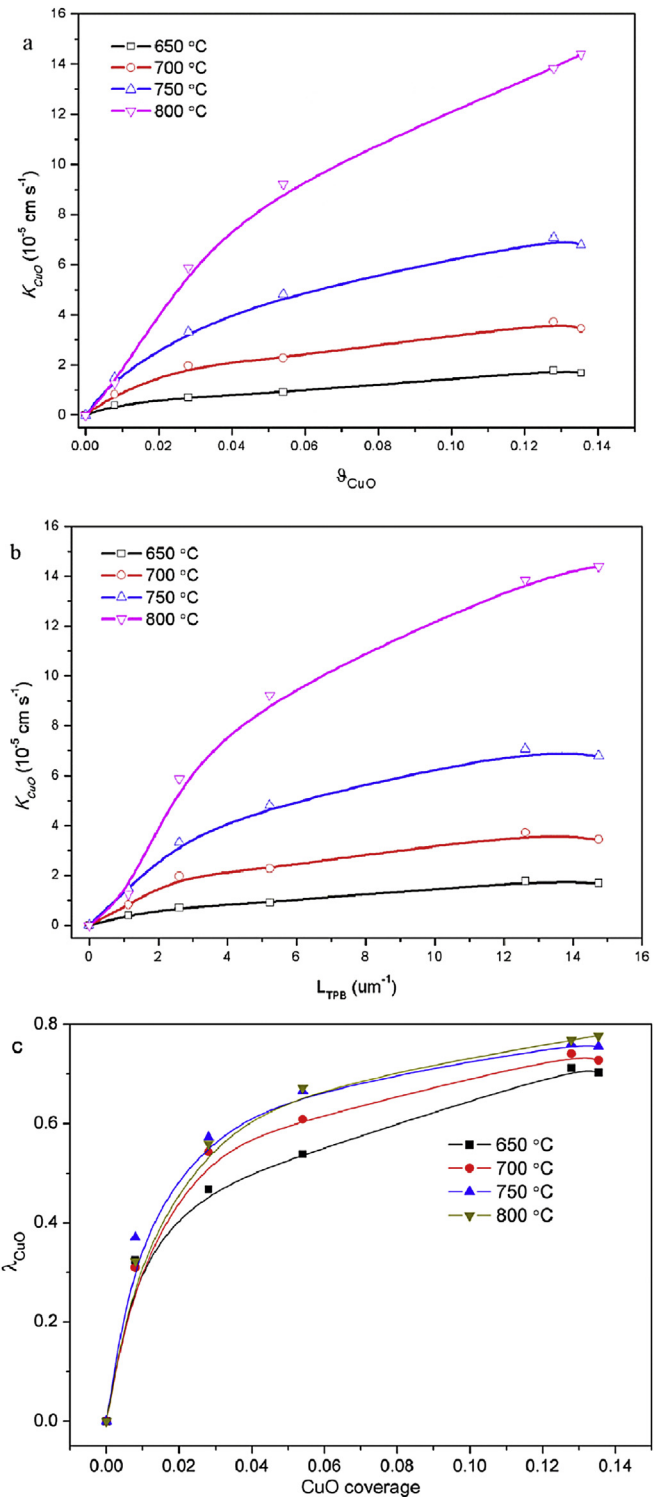

Fig. 3. The derived $k_{LSCF-CuO}$ plotted as a function of (a) θ_{CuO}, and (b) L_{3PB}. And (c) the contribution of CuO related reaction to the total oxygen incorporation.

experiment, the driving force condition is kept the same and the bulk transport properties are identical. Therefore, the reduced oxygen relaxation time is attributed to accelerated oxygen surface incorporated rate.

The relaxation profiles shown in Fig. 2a were used to obtain the effective oxygen surface exchange coefficient, k_{eff} (cm s^{-1}), which is defined for all the samples by assuming that the oxygen
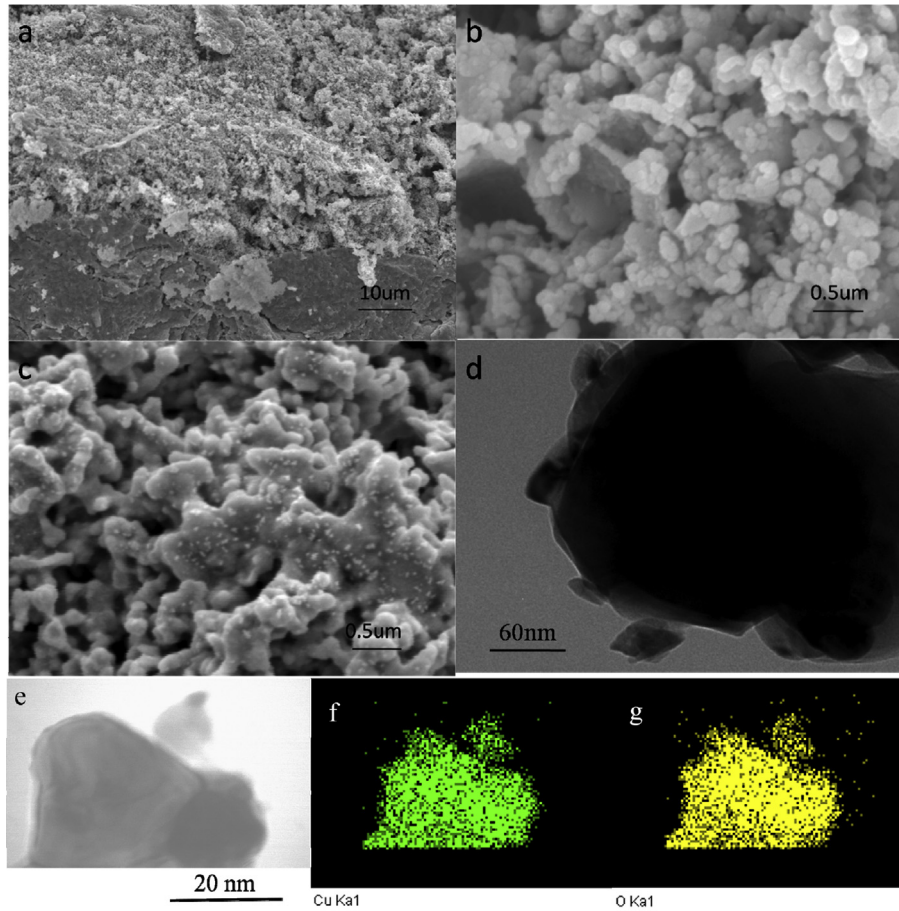
Fig. 4. Microstructure images for LSCF electrodes and CuO nanoparticles. (a) SEM for a bare LSCF electrode supported on a dense SDC electrolyte, (b) enlarge of LSCF electrode showing (a), (c) SEM for a LSCF infiltrated with 8.5 wt% CuO particles, (d) TEM showing 3 nanosized CuO particles on a microsized LSCF particle, and (e–g) TEM-EDS images for Cu and O element in a CuO nanoparticle.
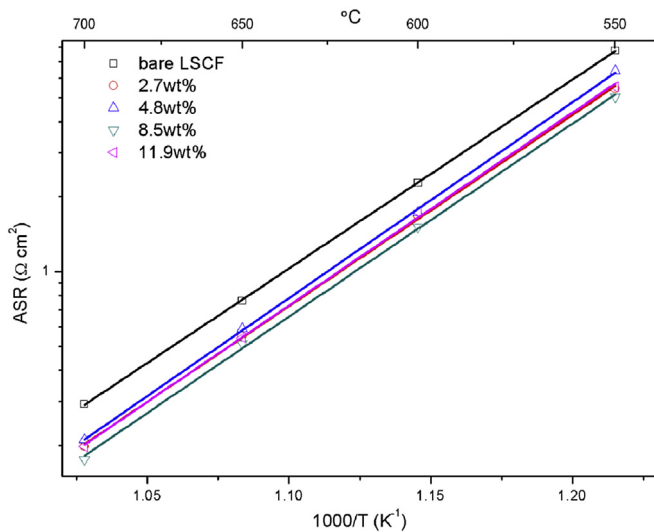
Fig. 5. Area surface polarization resistance (ASR) of an LSCF electrode infiltrated with various amounts of CuO particles.

incorporation reaction takes place homogenous on the surface. At 750 °C, the coefficient for the bare LSCF, k_{LSCF}, is 2.6×10^{-5} cm s^{-1}, which is consistent with the previous reported values, from 0.7 to

2.5×10^{-5} cm s^{-1} at the same temperature [15,16,28]. The variation in k_{LSCF} could be caused by the difference in grain size and grain boundary length resulting from various fabrication conditions. After the LSCF was decorated with CuO particles, k_{eff} increased up to 4.0×10^{-5} cm s^{-1} for sample CuO40, and further to 9.3×10^{-5} cm s^{-1} for the sample CuO120.

The enhanced oxygen incorporation kinetics, i.e. increased k_{eff}, is attributed to the presence of CuO particles. For the sample with CuO, k_{eff} is controlled by the reaction on pure LSCF surface and the reaction associated with CuO.

$$k_{eff} = k_{LSCF-CuO} + (1 - \theta)k_{LSCF} \qquad (1)$$

$k_{LSCF-CuO}$ can be obtained since θ is available from microstructural data presented in Table 1. The oxygen incorporation reaction associated with CuO particles may occur on the CuO particle surface and/or at the LSCF-CuO-gas 3PB. If it takes place only on the CuO surface, $k_{LSCF-CuO}$ should increase linearly with θ. On the other hand, if the reaction is confined to the boundaries, $k_{LSCF-CuO}$ must increase linearly with L_{3PB}.

From Fig. 3a and b, we can find that both $K_{LSCF-CuO}$ with θ_{CuO} and L_{3PB} display a non-linear relationship. With the increasing of θ_{CuO} and L_{3PB}, the increasing rate of $K_{LSCF-CuO}$ gradually decreases and reaches a value of 3.5×10^{-5} cm s^{-1} with θ_{CuO} of 0.13 and L_{TPB} of 14.74 μm^{-1}. This non-linear relationship suggests that the enhanced oxygen incorporation reaction may take place concurrently on CuO particle surface and LSCF-CuO-gas three phase

Table 2
The performance of LSCF electrodes infiltrated with various materials.

| Infiltrated material	Electrolyte	Performance	Improving factor f_P
7.5 µg cm^{-2} Pd [10]	GDC	700 °C ASR Infiltrated: 0.04 Ω cm^2 Bare: 0.14 Ω cm^2	3.5
1.2 mg cm^{-2} Pd [13]	GDC	600 °C ASR Infiltrated: 2.9 Ω cm^2 Bare: 5.4 Ω cm^2	1.86
Pd [11]	SDC	700 °C ASR Infiltrated: 0.247 Ω cm^2 Bare: 0.35 Ω cm^2	1.42
18 wt% Ag [8]	SDC	530 °C Power density Infiltrated: 0.42 W cm^{-2} Bare: 0.32 W cm^{-2}	1.31
Rh [11]	SDC	700 °C ASR Infiltrated: 0.261 Ω cm^2 Bare: 0.35 Ω cm^2	1.34
18 wt% Ag [8]	YSZ	630 °C Power density Infiltrated: 0.25 W cm^{-2} Bare: 0.16 W cm^{-2}	1.56
9.2 wt% BaCO$_3$ [20]	SDC	600 °C ASR Infiltrated: 0.94 Ω cm^2 Bare: 2.27 Ω cm^2	2.42
SDC [12]	SDC	700 °C ASR Infiltrated: 0.17 Ω cm^2 Bare: 0.4 Ω cm^2	2.35
1.5 mg cm^{-2} GDC [13]	GDC	600 °C ASR Infiltrated: 1.6 Ω cm^2 Bare: 5.4 Ω cm^2	3.38
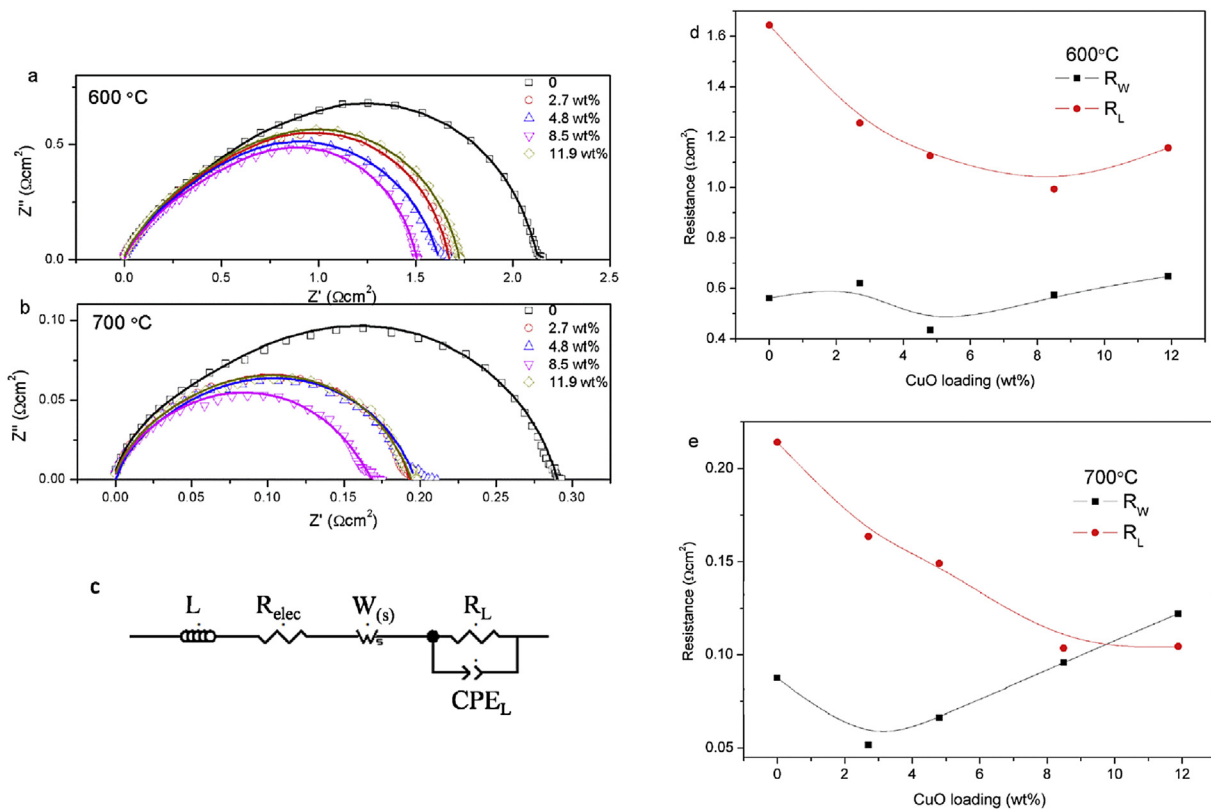
Fig. 6. Impedance spectra at (a) 600 °C and (b) 700 °C for LSCF electrode infiltrated with various amount of CuO, and (c) the fitting circuit. The fitting results (the lines) are shown on the spectra. (d) High frequency resistance (R_W) and (e) low frequency resistance (R_L) of CuO infiltrated LSCF electrodes.

boundary. The enhancement of the unit area and 3PB length gradually decreases as more CuO particles are added to the surface. However, details regarding the proportional contribution of each pathway is still a concern and needs to be addressed in future work.

The contribution ratio λ_{CuO} of CuO is used to represent the oxygen incorporation at CuO compared to the oxygen incorporating over the entire sample volume. λ_{CuO} is derived from the contribution of CuO by the following equation:
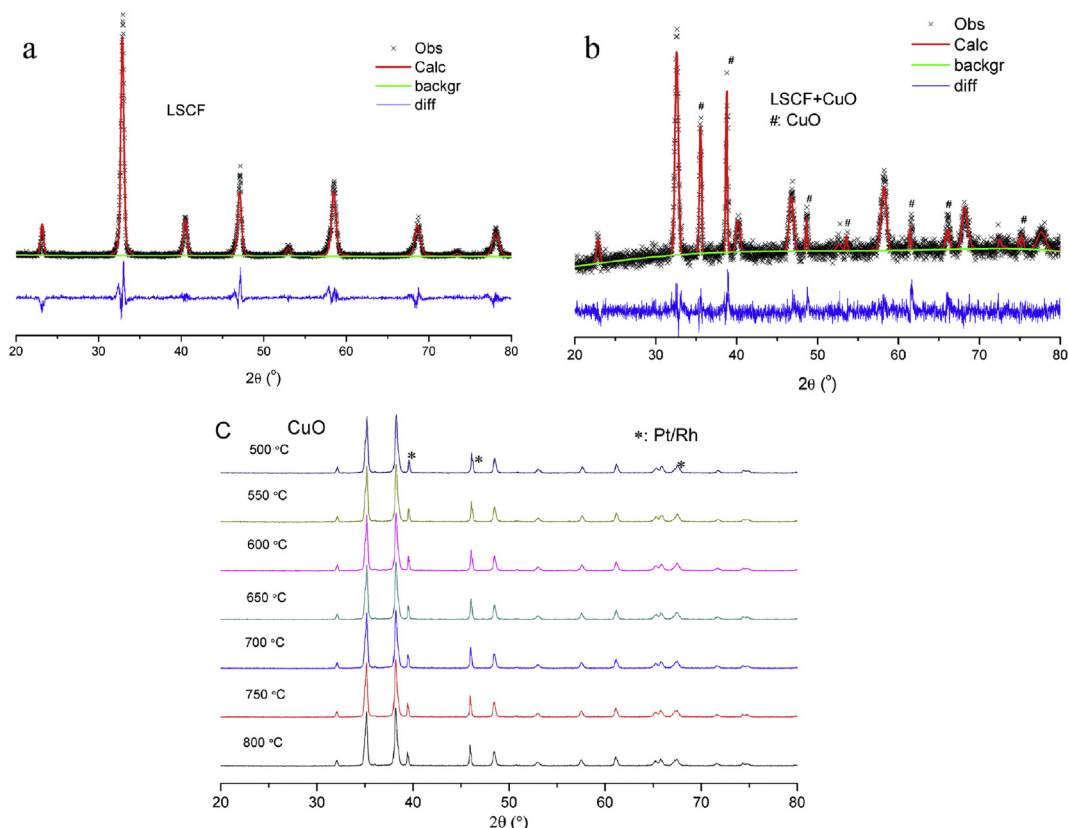
Fig. 7. The Rietveld refinement analysis of (a) LSCF powder and (b) LSCF + Cu(NO₃)₂ powders heated at 800 °C for 10 h, and (c) *in situ* X-ray of CuO at the temperature range of 500–800 °C.

$$\lambda = \frac{k_{LSCF-CuO}}{k_{eff}} \qquad (2)$$

Fig. 3d gives the relationship between the λ_{CuO} value and the CuO coverage area θ_{CuO}. It is seen that λ_{CuO} increases with increasing of CuO coverage. At a point where θ_{CuO} is 0.03, CuO already contributes over half of incorporated oxygen and eventually reaches a maximum of 78% when θ_{CuO} is 0.14. It is also noted that at fixed CuO coverage, λ_{CuO} is lager at higher temperature which suggests that the synergistic effect between CuO and LSCF becomes stronger at higher temperature.

3.3. Electrochemical performance of CuO decorated LSCF electrode

The ORR synergistic catalytic activity of CuO in LSCF was also examined using electrochemical impedance spectroscopy (EIS) measurements conducted on SDC electrolyte. Fig. 4a shows the typical microstructure of a bare LSCF electrode supported on a dense SDC electrolyte. The LSCF cathode consisted of grains with 0.2–0.3 μm in size, Fig. 4b. Fig. 4c reveals that very fine CuO particles were deposited on the LSCF surface after the infiltration treatment. The average size of the fine particle was approximately 40 nm, which is further confirmed with TEM analysis (Fig. 4d). Fig. 4e–g show the TEM-EDS images of CuO nanoparticles. The element mapping result of Cu and O could confirm that the nanoparticle is CuO.

Fig. 5 gives the area surface polarization resistance (ASR) value from 550 to 700 °C for LSCF electrodes impregnated with different amount of CuO. The ASR value of LSCF electrode goes through a considerable decrease after infiltration with CuO nanoparticles [29,30]. The resistance at 600 °C was 2.27 Ω cm² for the bare LSCF

electrode and decreased to 1.72 and 1.67 Ω cm² when the CuO loading weight increased from 2.7 wt% to 4.8 wt%. The lowest ASR value of 1.5 Ω cm² was achieved at loading of 8.5 wt% CuO. Further increase in the CuO loading weight (11.9 wt%) resulted in an increased ASR up to 1.73 Ω cm². When CuO applied as a single cathode in SDC electrolyte, the ASR values from 700 to 550 °C are 18.7, 55.7, 164 and 600 Ω cm² that are much larger than bare LSCF electrode. Table 2 gives the data for LSCF electrodes infiltrated with various materials reported in the literature. The electrode polarization resistance depends not only on the electro-catalyst activity but also on the microstructures of electrolyte and the electrode. So, direct comparison on the electrode resistance does not fully show the infiltration effect of different materials since their microstructures could be different as a result prepared via different processes and by various groups. The infiltration effect is compared using the performance improving factor, f_p, describe the enhancement on the catalytic activity of the electrode materials. For CuO, the improvement factor from 550 to 700 °C is between 1.54 and 1.67 when 8.5 wt% infiltrated CuO was used as a catalyst. These values are comparable with those reported for precious metal like Ag and Rh, which are believed to be excellent catalysts for ORR. But it is much lower than those reported for doped ceria, which are known to be excellent ionic conductor and improve the ORR through extending the three-phase boundary length.

3.4. Oxygen reduction steps

Fig. 6a–b shows the typical impedance spectra for the symmetric cells. The electrode reaction process of porous LSCF cathodes on doped ceria electrolytes have been carefully investigated by N. Grunbaum et al. [31] using the electrochemical impedance spectroscopy. They have proposed an electrical equivalent circuit for the
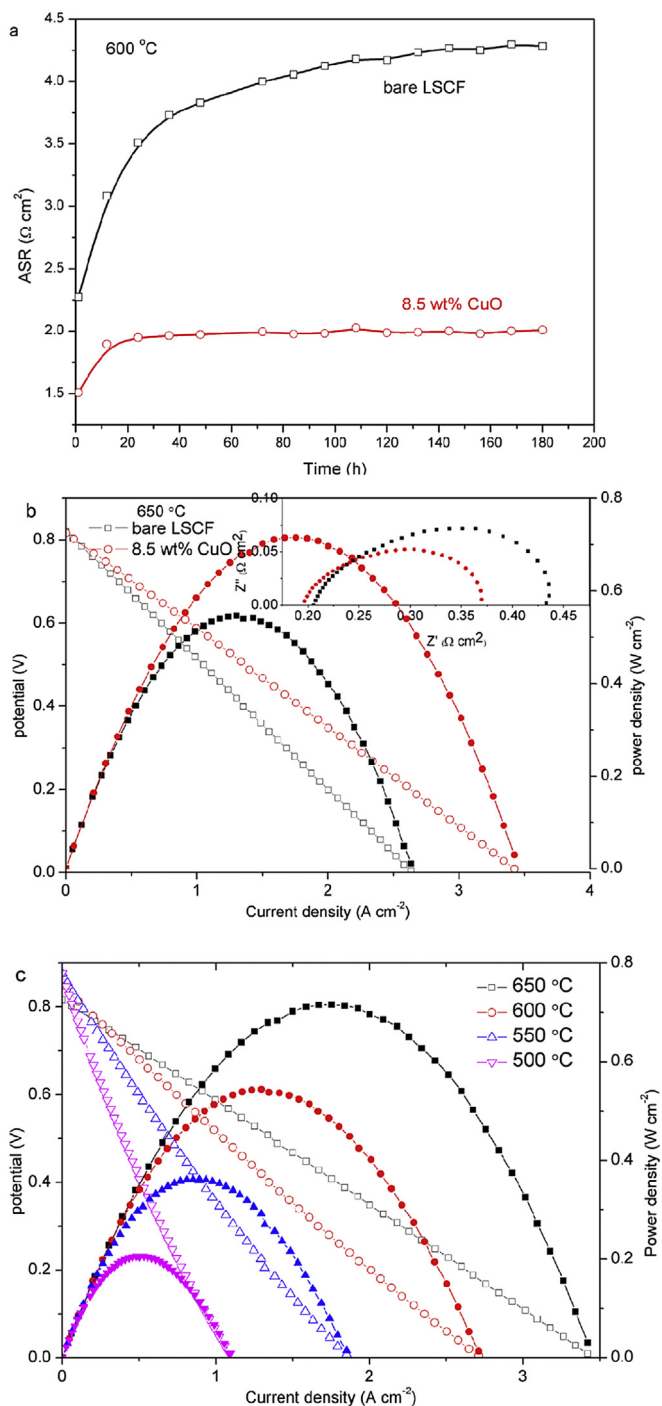
Fig. 8. (a) Long term stability of bare LSCF electrode and 8.5 wt% CuO infiltrated LSCF electrode, (b) *V-I* performance measured at 650 °C for anode-supported single cells with LSCF cathodes impregnated with 8.5 wt% CuO, and (c) cell performance of LSCF cathode impregnated with CuO at 500–650 °C.

electrical response of this system due to changing oxygen partial pressure over the range from 10^{-4} to 0.02 atm displayed in Fig. 6c. The equivalent circuit consists of a pure inductance (L) connected in series with a pure resistive element, R_{elec} representing the electrolyte resistance, a high-frequency Warburg impedance (W) and a circuit element consisting of a resistance (R_L) in parallel with a constant phase element (CPE). This last combination is used to fit the low-frequency range of the impedance diagram. The two-arc fitting lines match well with the experimental results, Fig. 6a–b

and the effect of CuO is clearly demonstrated by reduction of the spectra.

Fig. 6d–e shows the CuO loading effect on R_W and R_L measured at 600 and 700 °C. The fitted values for the bare LSCF are consistent with our previously reported results [32]. R_W is almost independent of the loading, demonstrating that CuO nanoparticle does not have obvious effects on the process associated with the high-frequency arc. Compared with that of the bare LSCF electrode, the impedance loop appearing at the low frequencies varys dramatically with the infiltration of CuO. For example, at 600 °C, R_L is 1.64 Ω cm² for the bare LSCF cathode. It decreases to 1.26 and 0.99 Ω cm² with 2.7 wt% and 8.5 wt% CuO respectively. The proportion of R_L in the ASR value was reduced from 72% to 63%. According to the model suggested by Maier et al. [33,34] and Liu et al. [35] for the LSCF electrodes, the high frequency feature can be assigned to the oxygen ion transfer across the interface between the cathode and the electrolyte, while the low frequency feature can be assigned to the electrochemical oxygen surface exchange reaction. Combined with the result in ECR experiment, CuO displays significant synergistic ORR catalytic activity on the LSCF surface. The greatly accelerated oxygen incorporation process contributes to the enhanced electrochemical performance of the LSCF electrode.

3.5. CuO phase structure

Fig. 7a and b displays the XRD Rietveld refinement analysis for LSCF single powder and LSCF-CuO composite powder sintered at 800 °C for 10 h. LSCF is well fitted and indicates standard perovskite structure in Fig. 7a. The cell parameters of LSCF single phase are a = b = 0.5475 nm, c = 1.347 nm, α = β = 90° and ϒ = 120°. In LSCF-CuO composite powder, all peaks are well fitted and could be attributed to either LSCF or CuO, Fig. 7b. The cell parameters of LSCF obtained from composite powder are a = b = 0.5471 nm, c = 1.349 nm, α = β = 90° and ϒ = 120°. This little difference is mainly due to higher error in composite phase fitting. So no obvious peak shifting and similar cell parameters suggests the lack of a chemical reaction between LSCF and CuO under the experimental conditions. And the particle size of CuO obtained from XRD data by Scherrer equation is 60 nm that is close to the size obtained by TEM image. Fig. 7c shows the *in situ* XRD results of CuO examined over the temperature range from 500 to 800 °C. CuO remains a stable phase with no trace of Cu_2O which has been reported as one possible reason for the catalytic activity in this material system [36,37].

CuO has been used as an ORR catalyst as discussed in previous part, however its catalytic activity is lower than LSCF [38,39], also as discussed in previous part. When discussing about the ORR catalytic activity of CuO and LSCF, we could find that due to lower ORR activity of CuO, coated CuO particles should reduce the surface area and thus reduce the *k* value of LSCF. While in the present work, there was a low coverage of CuO particles on the LSCF surface, and the observed enhancement in the ORR kinetics. Therefor the ORR activity in CuO infiltrated LSCF electrode is higher than bare LSCF or CuO, which means a promotion in both phase that could be defined as a synergistic catalytic activity of CuO on the LSCF surface.

3.6. Long term stability and single cell performance

Fig. 8a compares the stability of LSCF electrodes. When it is held at 600 °C for 180 h, the bare LSCF electrode goes through a persistent decline in electrochemical performance; the interfacial polarization resistance increases from 2.27 Ω cm² to 4.18 Ω cm² at 100 h and further to 4.28 Ω cm² at 180 h. The electrode with 8.5 wt% CuO shows much better performance; it increases from 1.51 Ω cm² to 2.0 Ω cm² at 100 h, and finally reaches 2.01 Ω cm² at 180 h which

is only 47% of bare LSCF electrode. This suggests the good stability of CuO infiltrate LSCF electrode compared to bare LSCF electrode and a steadiness of CuO against agglomeration at 600 °C. The single cell performance was evaluated for electrodes with CuO infiltrated LSCF. Fig. 8b shows the cell voltage and power density at 650 °C as a function of current density when humidified hydrogen was used as the fuel and ambient air as the oxidant. The peak power density for the cell with a bare LSCF cathode was 0.54 W cm^{-2}, which increased by 33.3% to 0.72 W cm^{-2} when the cathode was infiltrated with 8.5 wt% CuO. The improved power density must originate with the CuO particles since these cells have the same anodes and electrolytes. The impedance spectra measured under open-circuit conditions are shown in Fig. 8b. These cells have almost the same electrolyte resistances, about 0.20 Ω cm^2. The resistance was 0.21 Ω cm^2 for the single cell with a bare LSCF cathode which decreased to 0.15 Ω cm^2 when 8.5 wt% CuO was infiltrated. The performance date for this configuration (8.5 wt% CuO infiltrated cathode) is shown in Fig. 8c at 500–650 °C where peak power densities at 500, 550, 600 and 650 °C were 0.21, 0.36, 0.54 and 0.72 W cm^{-2} respectively.

4. Conclusions

This study demonstrates that a LSCF electrode surface decorated with CuO can strongly accelerate the ORR activity. The enhanced surface exchange was found to be non-linear relationship with respect to CuO area and LSCF-CuO-phase length which suggests that the enhanced oxygen reduction took place at both the CuO surface and CuO-LSCF-air boundary. In a CuO infiltrated LSCF electrode at 600 °C, the resistance was reduced from 2.27 to 1.5 Ω cm^2. These particles significantly reduced the low-frequency resistance that is associated with the surface reaction process. Furthermore, the particles improved the electrochemical performance of single cells with LSCF cathodes, leading to a 33% improvement in the peak power density. Future studies are necessary to achieve insights into the surface processes and features that govern the ORR activity in this material system.

Acknowledge

References

[1] S.B. Adler, Factors governing oxygen reduction in solid oxide fuel cell cathodes, Chem. Rev. 104 (2004) 4791–4844.
[2] A. Hauch, S.H. Jensen, S. Ramousse, M. Mogensen, Performance and durability of solid oxide electrolysis cells, J. Electrochem. Soc. 153 (2006) A1741–A1747.
[3] Y. Wang, T. Liu, S. Fang, G. Xiao, H. Wang, F. Chen, A novel clean and effective syngas production system based on partial oxidation of methane assisted solid oxide co-electrolysis process, J. Power Sources 277 (2015) 261–267.
[4] T.Z. Sholklapper, H. Kurokawa, C. Jacobson, S. Visco, L. De Jonghe, Nanostructured solid oxide fuel cell electrodes, Nano Lett. 7 (2007) 2136–2141.
[5] J.M. Vohs, R.J. Gorte, High-performance SOFC cathodes prepared by infiltration, Adv. Mater. 21 (2009) 943–956.
[6] T. Hong, L. Zhang, F. Chen, C. Xia, Oxygen surface exchange properties of La$_{0.6}$Sr$_{0.4}$Co$_{0.8}$Fe$_{0.2}$O$_{3-\delta}$ coated with Sm$_x$Ce$_{1-x}$O$_{2-\delta}$, J. Power Sources 218 (2012) 254–260.
[7] S.P. Jiang, Nanoscale and nano-structured electrodes of solid oxide fuel cells by infiltration: advances and challenges, Int. J. Hydrogen Energy 37 (2012) 449–470.
[8] Y. Sakito, A. Hirano, N. Imanishi, Y. Takeda, O. Yamamoto, Y. Liu, Silver infiltrated La$_{0.6}$Sr$_{0.4}$Co$_{0.2}$Fe$_{0.8}$O$_3$ cathodes for intermediate temperature solid oxide fuel cells, J. Power Sources 182 (2008) 476–481.
[9] S.P. Simner, M.D. Anderson, J.E. Coleman, J.W. Stevenson, Performance of a novel La (Sr) Fe (Co) O$_3$–Ag SOFC cathode, J. Power Sources 161 (2006)

[10] M. Sahibzada, S. Benson, R. Rudkin, J. Kilner, Pd-promoted La$_{0.6}$Sr$_{0.4}$Co$_{0.2}$Fe$_{0.8}$O$_3$ cathodes, Solid State Ion. 113 (1998) 285–290.
[11] J.M. Serra, H.-P. Buchkremer, On the nanostructuring and catalytic promotion of intermediate temperature solid oxide fuel cell (IT-SOFC) cathodes, J. Power Sources 172 (2007) 768–774.
[12] L. Nie, M. Liu, Y. Zhang, M. Liu, La$_{0.6}$Sr$_{0.4}$Co$_{0.2}$Fe$_{0.8}$O$_3$ cathodes infiltrated with samarium-doped cerium oxide for solid oxide fuel cells, J. Power Sources 195 (2010) 4704–4708.
[13] J. Chen, F. Liang, B. Chi, J. Pu, S.P. Jiang, L. Jian, Palladium and ceria infiltrated La$_{0.8}$Sr$_{0.2}$Co$_{0.5}$Fe$_{0.5}$O$_3$ cathodes of solid oxide fuel cells, J. Power Sources 194 (2009) 275–280.
[14] D. Ding, X. Li, S.Y. Lai, K. Gerdes, M. Liu, Enhancing SOFC cathode performance by surface modification through infiltration, Energy Environ. Sci. 7 (2014) 552–575.
[15] B. Hu, Y. Wang, C. Xia, Oxygen incorporation at the three-phase boundary of LSCF–SDC composite, J. Power Sources 269 (2014) 180–188.
[16] B. Hu, Y. Wang, C. Xia, Effects of ceria conductivity on the oxygen incorporation at the LSCF-SDC-gas three-phase boundary, J. Electrochem. Soc. 162 (2015) F33–F39.
[17] Y. Liang, Y. Li, H. Wang, J. Zhou, J. Wang, T. Regier, H. Dai, Co$_3$O$_4$ nanocrystals on graphene as a synergistic catalyst for oxygen reduction reaction, Nat. Mater. 10 (2011) 780–786.
[18] T. Hong, F. Chen, C. Xia, Barium carbonate nanoparticle to enhance oxygen reduction activity of strontium doped lanthanum ferrite for solid oxide fuel cell, J. Power Sources 278 (2015) 741–750.
[19] T. Hong, F. Chen, C. Xia, Barium carbonate nanoparticle as high temperature oxygen reduction catalyst for solid oxide fuel cell, Electrochem. Commun. 51 (2015) 93–97.
[20] C. Xia, T. Hong, K. Brinkman, Barium carbonate nanoparticles as synergistic catalysts for the oxygen reduction reaction on La$_{0.6}$Sr$_{0.4}$Co$_{0.2}$Fe$_{0.8}$O$_{3-\delta}$ solid oxide fuel cell cathodes, ChemElectroChem 3 (2016) 805–813.
[21] S. Imamura, Y. Tsuji, Y. Miyake, T. Ito, Cooperative action of palladium and manganese (III) oxide in the oxidation of carbon monoxide, J. Catal. 151 (1995) 279–284.
[22] M. Kahlich, H. Gasteiger, R. Behm, Kinetics of the selective low-temperature oxidation of CO in H$_2$-Rich gas over Au/α-Fe$_2$O$_3$, J. Catal. 182 (1999) 430–440.
[23] J. Jansson, A.E. Palmqvist, E. Fridell, M. Skoglundh, L. Österlund, P. Thormählen, V. Langer, On the catalytic activity of Co$_3$O$_4$ in low-temperature CO oxidation, J. Catal. 211 (2002) 387–397.
[24] C.L. Chang, C.C. Hsu, T.J. Huang, Cathode performance and oxygen-ion transport mechanism of copper oxide for solid-oxide fuel cells, J. Solid State Electrochem. 7 (2003) 125–128.
[25] L. Lu, Q. Shi, Y. Yang, H. Zhang, Electrochemical performance of (La, Sr)(Co, Fe) O$_{3-\delta}$–(Ce, Sm) O$_{2-\theta}$ –CuO composite cathodes for intermediate temperature solid oxide fuel cells, Mater. Res. Bull. 47 (2012) 1016–1020.
[26] J. Martynczuk, M. Arnold, H. Wang, J. Caro, A. Feldhoff, How (Ba$_{0.5}$Sr$_{0.5}$)(Fe$_{0.8}$Zn$_{0.2}$)O$_{3-\delta}$ and (Ba$_{0.5}$Sr$_{0.5}$)(Co$_{0.8}$Fe$_{0.2}$)O$_{3-\delta}$ perovskites form via an EDTA/ citric acid complexing method, Adv. Mater. 19 (2007) 2134–2140.
[27] J. Lane, J. Kilner, Measuring oxygen diffusion and oxygen surface exchange by conductivity relaxation, Solid State Ionics 136 (2000) 997–1001.
[28] H. Bouwmeester, M. Den Otter, B. Boukamp, Oxygen transport in La$_{0.6}$Sr$_{0.4}$Co$_{1-y}$Fe$_y$O$_{3-\delta}$, J. Solid State Electrochem. 8 (2004) 599–605.
[29] Y. Zhang, M. Ni, C. Xia, Microstructural insights into dual-phase infiltrated solid oxide fuel cell electrodes, J. Electrochem. Soc. 160 (2013) F834–F839.
[30] Y. Zhang, Q. Sun, C. Xia, M. Ni, Geometric properties of nanostructured solid oxide fuel cell electrodes, J. Electrochem. Soc. 160 (2013) F278–F289.
[31] N. Grunbaum, L. Dessemond, J. Fouletier, F. Prado, L. Mogni, A. Caneiro, Rate limiting steps of the porous La$_{0.6}$Sr$_{0.4}$Co$_{0.8}$Fe$_{0.2}$O$_{3-\delta}$ electrode material, Solid State Ion. 180 (2009) 1448–1452.
[32] Y. Wang, L. Zhang, F. Chen, C. Xia, Effects of doped ceria conductivity on the performance of La$_{0.6}$Sr$_{0.4}$Co$_{0.2}$Fe$_{0.8}$O$_{3-\delta}$ cathode for solid oxide fuel cell, Int. J. Hydrogen Energy 37 (2012) 8582–8591.
[33] F.S. Baumann, J. Fleig, M. Konuma, U. Starke, H.-U. Habermeier, J. Maier, Strong performance improvement of La$_{0.6}$Sr$_{0.4}$Co$_{0.8}$Fe$_{0.2}$O$_{3-\delta}$ SOFC cathodes by electrochemical activation, J. Electrochem. Soc. 152 (2005) A2074–A2079.
[34] F.S. Baumann, J. Fleig, H.U. Habermeier, J. Maier, Impedance spectroscopic study on well-defined (La, Sr)(Co, Fe) O$_{3-\delta}$ model electrodes, Solid State Ion. 177 (2006) 1071–1081.
[35] J.W. Lee, Z. Liu, L. Yang, H. Abernathy, S.-H. Choi, H.-E. Kim, M. Liu, Preparation of dense and uniform La$_{0.6}$Sr$_{0.4}$Co$_{0.2}$Fe$_{0.8}$O$_{3-\delta}$ (LSCF) films for fundamental studies of SOFC cathodes, J. Power Sources 190 (2009) 307–310.
[36] A. Martínez-Arias, M. Fernández-García, O. Gálvez, J. Coronado, J. Anderson, J. Conesa, J. Soria, G. Munuera, Comparative study on redox properties and catalytic behavior for CO oxidation of CuO/CeO$_2$ and CuO/ZrCeO$_4$ catalysts, J. Catal. 195 (2000) 207–216.
[37] R. Molinari, T. Poerio, P. Argurio, Liquid-phase oxidation of benzene to phenol using CuO catalytic polymeric membranes, Desalination 241 (2009) 22–28.
[38] M. Pena, J. Fierro, Chemical structures and performance of perovskite oxides, Chem. Rev. 101 (2001) 1981–2018.
[39] K. Zhou, R. Wang, B. Xu, Y. Li, Synthesis, characterization and catalytic properties of CuO nanocrystals with various shapes, Nanotechnology 17 (2006) 3939.